

# Fluorine-Free Bis(glycolato)borate Anion-Based Salts and Electrolytes: Structures, Properties, and Lithium Compatibility

Yanqi Xu,<sup>[a]</sup> Andrei Filippov,<sup>[a]</sup> Manishkumar R. Shimpi,<sup>[b]</sup> Faiz Ullah Shah,\*<sup>[a]</sup> and Patrik Johansson\*,<sup>[c, d]</sup>

A number of bis(glycolato)borate (BGB) anion-based salts, comprising Li<sup>+</sup>, Na<sup>+</sup>, K<sup>+</sup>, Mg<sup>2+</sup> and Ca<sup>2+</sup> cations, has been synthesized and characterized. Fluorine-free electrolytes based on LiBGB and organic solvents, such as dimethyl sulfoxide (DMSO), triethyl phosphate (TEP), and trimethyl phosphate (TMP) have been created and their transport properties, thermal and electrochemical stabilities, and lithium compatibility are examined. The ionic conductivities of the 1 M LiBGB-TEP and 1 M LiBGB-TMP electrolytes are ca. 2–3 times lower than for the 1 M LiBGB-DMSO electrolytes (2.05, 2.65 vs. 5.70 mS cm<sup>-1</sup> at 25 °C), and as compared to the state-of-the-art 1 M lithium hexafluorophosphate (LiPF<sub>6</sub>) in EC:DEC (EC:DEC = 1:1 in vol.,

LP40) they display lower ionic conductivities, but the formers' redox stability on aluminum (Al) and glassy carbon electrodes are much better. Concentrated (> 1 M) LiBGB-DMSO electrolytes display enhanced redox stability, but worse Al passivation. Among the electrolytes, 1 M LiBGB-TMP achieves the best long-term stability over 300 h at 0.1 mA/cm<sup>2</sup> for Li plating-stripping while the Li compatibility needs to be further improved. Overall, this study introduces a family of versatile fluorine-free orthoborate salts and electrolytes for mono- and divalent batteries, and a fundamental understanding of their transport and electrochemical properties, aiming towards battery applications.

## Introduction

The unique chemistry of boron brings structural versatility useful for a range of applications, in particular for sustainable and clean energy<sup>[1–3]</sup> as well as rechargeable batteries.<sup>[4–7]</sup> As for the latter, boron-based salts such as lithium/sodium tetrafluoroborate (Li/NaBF<sub>4</sub>),<sup>[8–10]</sup> lithium/sodium bis(oxalato)borate (Li/NaBOB),<sup>[4,6,11,12]</sup> lithium/sodium difluoro(oxalato)borate (Li/NaDFOB)<sup>[13–16]</sup> have all been widely studied as lithium-ion battery (LIB) and sodium-ion battery (SIB) electrolytes, with promising performance for different battery technologies.<sup>[6,15,17,18]</sup> Among these borate salts, especially BOB

anion-based salts have been extensively explored in terms of crystallography,<sup>[19,20]</sup> physicochemical and electrochemical properties<sup>[21,22]</sup> as well as for practical battery cell performance.<sup>[4,7,23]</sup> In practical studies, Roy *et al.*<sup>[17]</sup> introduced the moisture-stable lithium 1,1,1,3,3,3-(tetrakis)hexafluoroisopropoxy borate (Li[B(hfip)<sub>4</sub>]) salt, which displayed excellent oxidation stability vs. different electrodes and also excellent passivation of aluminum (Al) at high voltages, and Min *et al.*<sup>[24]</sup> reported on lithium difluoro(1,2-dihydroxyethane-1,1,2,2-tetracarbonitrile) borate (LiDFTCB) with an emphasis on the crucial role of the anion in promoting adequate battery cycling performance and safety. More recently, a variety of boron-containing calcium (Ca) and magnesium (Mg) salts, such as calcium tetrafluoroborate (Ca(BF<sub>4</sub>)<sub>2</sub>),<sup>[25]</sup> calcium borohydride (Ca(BH<sub>4</sub>)<sub>2</sub>),<sup>[26]</sup> magnesium borohydride (Mg(BH<sub>4</sub>)<sub>2</sub>),<sup>[27]</sup> etc. have been investigated for multivalent batteries, where the presence of boron seems very crucial, while its exact role is not fully understood.<sup>[5,28,29]</sup>

Many of the boron-based salts above, however, also contain large amounts of fluorine, that while offering beneficial properties in terms of battery performance, create problems at all stages from synthesis to usage and even at the recycling stages.<sup>[30,31]</sup> Yet, there exists a number of fluorine-free borate salts apart from BOB, such as lithium bis(salicylato)borate (LiBScB),<sup>[32]</sup> lithium bis(1,2-benzenediolato)borate (LiBB)<sup>[32]</sup> and these and other similar anions have primarily been explored computationally; Johansson<sup>[33]</sup> computed the cation-anion interactions for some well-known boron-based anions, while Jankowski *et al.*<sup>[34]</sup> computationally introduced 15 new tetrahedral boron-centered Hückel anions.

[a] Y. Xu, A. Filippov, F. Ullah Shah

Chemistry of Interfaces, Luleå University of Technology, SE-971 87 Luleå, Sweden  
E-mail: faiz.ullah@ltu.se

[b] M. R. Shimpi

Department of Materials and Environmental Chemistry, Stockholm University, Stockholm, SE-114 18 Sweden

[c] P. Johansson

Department of Physics, Chalmers University of Technology, SE-412 96 Gothenburg, Sweden

[d] P. Johansson

ALISTORE-European Research Institute, FR CNRS 3104, Hub de l'Energie 15, Rue Baudelocque, 80039 Amiens, France  
E-mail: patrik.johansson@chalmers.se

Supporting information for this article is available on the WWW under <https://doi.org/10.1002/batt.202400672>

© 2024 The Author(s). *Batteries & Supercaps* published by Wiley-VCH GmbH. This is an open access article under the terms of the Creative Commons Attribution Non-Commercial NoDerivs License, which permits use and distribution in any medium, provided the original work is properly cited, the use is non-commercial and no modifications or adaptations are made.

As for BOB, Mogensen *et al.*<sup>[12]</sup> recently experimentally explored 0.5 M NaBOB in trimethyl phosphate (TMP) as a non-flammable and fluorine-free electrolyte with promising battery performance for SIBs. In general though, the Li/NaBOB salts are hydrolytically unstable and decompose when exposed to traces of moisture, and the decomposition products increase the battery cell impedance and thus adversely affect the overall battery performance.<sup>[23,35]</sup>

Here we introduce a family of orthoborate-based fluorine-free salts and electrolytes, all based on the bis(glycolato)borate (BGB) anion, which is a structural analogue of BOB (Figure 1). The concept of chelated orthoborate salt electrolytes is not new; for example, Barthel *et al.* reported on several thermally and electrochemically stable electrolytes based on lithium bis[1,2-benzenediolato(2-O,O')]borate,<sup>[36]</sup> lithium bis[tetrafluoro-1,2-benzenediolato(2-O,O')]borate,<sup>[37]</sup> lithium bis[2,3-naphthalenediolato(2-O,O')]borate,<sup>[37]</sup> and lithium bis[2,3-pyridinediolato(2-O,O')]borate.<sup>[38]</sup> However, all these orthoborate salts are based on bulky and/or fluorinated ligands, while in contrast to all the reported chelated orthoborate anions including BOB, BGB anion comprises only two carbonyl groups, provides extraordinary moisture and thermal stability of its salts. In this work, physicochemical and electrochemical properties of BGB-based salts and their resulting lithium conducting electrolytes, made using dimethyl sulfoxide (DMSO), triethyl phosphate (TEP) and trimethyl phosphate (TMP) as solvents, are thoroughly investigated and presented.

## Experimental

### Synthesis

The BGB anion-based salts,  $M[BGB]_n$ , ( $M=Li, Na, K, Mg, Ca; n=1, 2$ ), have all been prepared using water as a solvent at ambient and/or slightly elevated temperature from readily available starting materials. The precursors are cost-effective and green, and the reactions are performed following the principles of green chemistry.<sup>[39]</sup>

### Alkali Metal Salts

The synthesis of **LiBGB** and **NaBGB** started from mixing aqueous solutions of 0.1 mol glycolic acid ( $C_2H_4O_3$ , Sigma-Aldrich,  $\geq 99\%$ ) and 0.05 mol boric acid ( $H_3BO_3$ , Sigma-Aldrich,  $\geq 99.5\%$ ), followed by stirring for 30 min at ambient temperature. Then 0.05 mol of either lithium hydroxide monohydrate ( $LiOH \cdot H_2O$ , Sigma-Aldrich,  $\geq 98.0\%$ ) or sodium hydroxide ( $NaOH$ , Sigma-Aldrich,  $\geq 98.0\%$ ) was added to the reaction mixture and continuously stirred for 24 h at ambient temperature. In the case of **KBGB**, the reaction mixture was stirred at  $60^\circ C$  for 24 h. The water was rotary evaporated to get the product as a white powder. The crude products of **LiBGB**

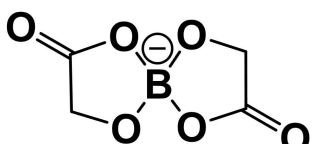


Figure 1. Chemical structure of the bis(glycolato)borate (BGB) anion.

and **NaBGB** salts were washed with acetonitrile (ACN, Sigma-Aldrich,  $\geq 99.5\%$ ) for at least 2–3 times to remove any unreacted precursors or impurities. For **KBGB**, ethyl acetate was used to remove any unreacted precursors or impurities. Finally, the products were dried in a vacuum oven at  $120^\circ C$  for 2 days.

### LiBGB

White solid. Yield: 98 %.  $^1H$  NMR (400.21 MHz, DMSO-d6)  $\delta$  3.94 (s, 4H) ppm.  $^{13}C$  NMR (100.64 MHz, DMSO-d6)  $\delta$  177.56, 65.54 ppm.  $^{11}B$  NMR (128.40 MHz, DMSO-d6): 11.35 ppm.  $^7Li$  NMR (155.54 MHz, DMSO-d6): -1.20 ppm.

### NaBGB

White solid. Yield: 93 %.  $^1H$  NMR (400.21 MHz, DMSO-d6)  $\delta$  3.96 (s, 4H) ppm.  $^{13}C$  NMR (100.64 MHz, DMSO-d6)  $\delta$  177.74, 65.56 ppm.  $^{11}B$  NMR (128.40 MHz, DMSO-d6): 11.37 ppm.  $^{23}Na$  NMR (105.86 MHz, DMSO-d6): -0.58 ppm.

### KBGB

White solid. Yield: 90 %.  $^1H$  NMR (400.21 MHz, DMSO-d6)  $\delta$  3.94 (s, 4H) ppm.  $^{13}C$  NMR (100.64 MHz, DMSO-d6)  $\delta$  177.56, 65.55 ppm.  $^{11}B$  NMR (128.40 MHz, DMSO-d6): 11.37 ppm.

### Alkaline Earth Metal Salts

For synthesis of  $Mg[BGB]_2$  and  $Ca[BGB]_2$  salts, 0.1 mol glycolic acid and 0.05 mol boric acid were dissolved in 100 mL  $H_2O$  and stirred for 30 min at  $60^\circ C$ , followed by addition of either 0.025 mol magnesium hydroxide ( $Mg(OH)_2$ , KEBO AB,  $\geq 95\%$ ) or calcium hydroxide ( $Ca(OH)_2$ , Sigma-Aldrich,  $\geq 95\%$ ) to the reaction mixture. The reaction mixture was stirred at  $60^\circ C$  for 24 h. The water was evaporated, and the product was washed with ethyl acetate for at least 5 times and finally the products were dried in a vacuum oven at  $120^\circ C$  for 2 days.

### $Mg[BGB]_2$

White solid. Yield: 90 %.  $^1H$  NMR (400.21 MHz, DMSO-d6)  $\delta$  3.94 (s, 4H) ppm.  $^{13}C$  NMR (100.64 MHz, DMSO-d6)  $\delta$  177.54, 65.54 ppm.  $^{11}B$  NMR (128.40 MHz, DMSO-d6): 11.39 ppm.

### $Ca[BGB]_2$

White solid. Yield: 87 %.  $^1H$  NMR (400.21 MHz, DMSO-d6)  $\delta$  3.93 (s, 4H) ppm.  $^{13}C$  NMR (100.64 MHz, DMSO-d6)  $\delta$  177.56, 65.53 ppm.  $^{11}B$  NMR (128.40 MHz, DMSO-d6): 11.45 ppm.

### Electrolyte Preparation

The solubility of **LiBGB** salt was tested in ten different solvents (Table S1), and four solvents: dimethyl sulfoxide (DMSO), triethyl phosphate (TEP), *N*-Methyl-2-pyrrolidone (NMP) and trimethyl phosphate (TMP) were found to dissolve this salt to form 1 molar (M) solutions, while it cannot be dissolved in EC-DMC (EC:DMC = 50:50 vol.:vol.) to create 1 M solution. Due to the high toxicity of NMP,<sup>[40,41]</sup> this solvent was excluded from further experiments. The electrolytes were prepared in an argon-filled glovebox (Mbraun EASYlab,  $H_2O$  and  $O_2 < 1\text{ ppm}$ ). Anhydrous DMSO (Sigma-Aldrich,  $\geq 99.9\%$ ), TEP (Sigma-Aldrich,  $\geq 99.8\%$ ), and TMP (Sigma-Aldrich,  $\geq 99\%$ ) were passed through 4 Å molecular sieves (Aldrich) that

were regenerated at 350 °C for 12 h. The LiBGB salt was dried in a vacuum oven at 120 °C for at least 2 days before transferring to the glovebox. For LiBGB in DMSO, the maximum room temperature solubility was 2.5 M, while for TEP and TMP it was ~1 M. The water contents of the prepared electrolytes were found to be <40 ppm as measured by Metrohm Karl-Fisher titration using a 917 coulometer. The benchmark electrolyte, 1 M LiPF<sub>6</sub> in EC-DEC (LP40, EC:DEC = 50:50 vol.vol., Sigma-Aldrich, battery grade) was used as received.

### NMR Spectroscopy

Solution-state multinuclear (<sup>1</sup>H, <sup>13</sup>C, <sup>11</sup>B, <sup>7</sup>Li and <sup>23</sup>Na) nuclear magnetic resonance (NMR) spectroscopy was performed using a Bruker Ascend Aeon WB 400 (Bruker BioSpin AG, Fällanden, Switzerland) spectrometer. The working frequencies were 400.21 MHz for <sup>1</sup>H, 128.40 MHz for <sup>11</sup>B, 100.64 MHz for <sup>13</sup>C, 155.54 MHz for <sup>7</sup>Li, and 105.86 MHz for <sup>23</sup>Na. The sample was dissolved in DMSO-d<sub>6</sub> and placed in a 5-mm standard glass tube.

### NMR Diffusometry

Pulse gradient spin echo nuclear magnetic resonance (PGSE-NMR) experiments were carried out on <sup>1</sup>H, on <sup>7</sup>Li, and on <sup>11</sup>B with a PGSE-NMR probe Diff50 (Bruker). Diffusional decays (DDs) of these nuclei were recorded using the stimulated echo (STE) pulse train. For a single-component diffusion, the form of the DD can be described by Equation (1).

$$A(\tau, \tau_1, g, \delta) \propto \exp\left(-\frac{2\tau}{T_2} - \frac{\tau_1}{T_1}\right) \exp(-\gamma^2 \delta^2 D t_d) \quad (1)$$

Here,  $A$  is the integral intensity of the NMR signal,  $\tau$  is the time interval between the first and the second radiofrequency pulses,  $\tau_1$  is the time interval between the second and the third radio-frequency pulses,  $T_1$  and  $T_2$  are longitudinal and transverse NMR relaxation times, respectively.  $\gamma$  is the gyromagnetic ratio for the magnetic nuclei of particular type;  $g$  and  $\delta$  are the amplitude and the duration of the gradient pulse;  $t_d(\Delta - \delta/3)$  is the diffusion time;  $\Delta$  is the time interval between two identical gradient pulses and  $D$  is the diffusion coefficient of the component. In all the PGSE-NMR experiments, the duration of the 90° pulse was 7 μs,  $\delta$  was in the range of (0.5–2) ms,  $\tau$  was in the range of (3–5) ms, and  $g$  was varied from 0.06 up to the maximum of the gradient amplitude, 29.73 T m<sup>-1</sup>. The diffusion time  $t_d$  was varied from 4 to 300 ms for all the nuclei. The repetition time during accumulation of signal transients was 3.5 s. Each measurement was repeated at least three times to ensure reproducibility.

### Single-Crystal X-Ray Diffraction

Deionized H<sub>2</sub>O was used to recrystallize LiBGB and NaBGB. The single-crystal X-ray diffraction (SXRD) data were collected using a Bruker D8 Venture equipped with a PHOTON 100 CMOS detector. Data collection was performed using  $\Phi$  and  $\omega$  scans. The crystals were quite stable and hence no extraordinary precautions were necessary for smooth collection of the intensity data. All the data were collected using MoK $\alpha$  radiation ( $\lambda = 0.71073$  Å), and the crystal structures were solved by using intrinsic phasing method followed by full-matrix least-squares refinement against F2 using SHELXTL. The data reduction was performed using a program package SAINT and the absorption corrections were carried out with the program SADABS. All the non-hydrogen atoms were refined by anisotropic method and the hydrogen atoms were refined and placed in

respected positions. All the structural refinements converged to good R-factors (Table S2). The structure, refinement, and generation of material for publication were performed by using the shelXL software.<sup>[42]</sup> The packing diagrams were generated by using the Diamond (version 4.6.1) software.<sup>[43]</sup>

### Moisture Sensitivity

For LiBGB and NaBGB *ca.* 1 g of freshly prepared salts were placed in an open container and covered with a perforated aluminum foil to keep the sample in contact with moisture (Figure S21a); exposed to humid air (20–30%) at 20–25 °C for up to 8 weeks. The salts were analyzed using <sup>1</sup>H, <sup>11</sup>B, <sup>13</sup>C, <sup>7</sup>Li and <sup>23</sup>Na NMR spectroscopies before and after exposure.

For moisture stability assessment of the fluorine-free lithium electrolytes, 1 M and 2 M LiBGB-DMSO were selected and *ca.* 1 mL of each fresh electrolyte was placed in a 5 mL vial and covered with a perforated aluminum foil to allow contact with moisture and also prevent evaporation (Figure S21b). The electrolytes were exposed to humid air (20–30%) at 20–25 °C for up to 4 weeks, and the benchmarked vs. *ca.* 1 mL of 1 M LiPF<sub>6</sub> in EC-DEC exposed to air for 24 h (where the glass became etched due to the formation of HF, as reported previously<sup>[17]</sup>). The fluorine-free electrolytes were analyzed using <sup>1</sup>H, <sup>11</sup>B, <sup>7</sup>Li and <sup>23</sup>Na NMR before and after exposure.

### Thermal Analyses

Thermal gravimetric analysis (TGA) and differential thermogravimetry (DTG) were carried out on a PerkinElmer TGA8000 instrument. Prior to any experiments, the samples were dried in a vacuum oven at 120 °C for 2 days and about 3–5 mg of sample was placed in a ceramic crucible and the temperature was increased from 30 °C to 600 °C at a heating rate of 10 °C per min. The melting points of the salts were assessed by an Electrothermal IA9000 Series Melting Point Apparatus up to 400 °C before carrying out differential scanning calorimetry (DSC). A PerkinElmer DSC6000 instrument was used for DSC experiments. For each experiment, *ca.* 2–6 mg of sample was sealed in an aluminum pan and all experiments were performed under N<sub>2</sub> atmosphere to exclude contact with moisture or air. Specifically, DSC experiments were carried out from –75 °C to +200 °C at a heating rate of 5 °C per min. The intersection of the baseline and the tangent was determined using the Pyris software to obtain the onset of the decomposition temperature ( $T_{decomp}$ ) and the glass transition temperature ( $T_g$ ).

### Electrochemical Assessments

Ionic conductivity measurements and linear sweep voltammetry (LSV) were made using a Metrohm Autolab PGSTAT302 N electrochemical workstation (Metrohm, Switzerland) with an FRA32 M module and a Nova 2.1.6 software. 70 μL of sample was packed in a closed TSC 70 cell coupled to a temperature-controller Microcell HC (rhd Instruments, Germany). The LSV experiments were performed at 20 °C at a scan rate of 1 mV s<sup>-1</sup> using a three-electrode configuration; a glassy carbon (GC, diameter = 2 mm) as the working electrode (WE), a 70 μL Pt crucible as sample container as well as counter electrode (CE), and an Ag wire coated with AgCl (Ag/AgCl) as a pseudo reference electrode (RE). Ferrocene (Fc/Fc<sup>+</sup>) was used as internal reference and the  $E_{Fc/Fc}^+$  potential was converted to  $E_{Li/Li}^+$  by +3.25 V.<sup>[44]</sup> A cut-off current density of ±0.1 mA cm<sup>-2</sup> was used to define the anodic and cathodic stabilities.

Ionic conductivities were determined using electrochemical impedance spectroscopy (EIS) from 1 Hz to 1 MHz frequency with an AC voltage amplitude of 10 mV<sub>rms</sub> in the temperature range from –25

to 100 ( $\pm 0.1$ ) °C. A two-electrode configuration was used: GC as WE and the Pt crucible as CE. A 100  $\mu\text{S}\text{cm}^{-1}$  KCl standard solution from Metrohm was applied to determine the cell constant ( $K_{\text{cell}} = 1.8736 \text{ cm}^{-1}$ ). The cell was thermally equilibrated for 10 min before data recording. Prior to each electrochemical experiment, the electrodes were polished using a Kemet diamond paste (average diameter = 0.25  $\mu\text{m}$ ).

For battery tests, CR2032 type coin cells were used. LSV and chronoamperometry (CA) were employed for assessing oxidation stability of the electrolytes on an aluminum (Al) substrate, Li plating-striping and the corresponding EIS using a Biologic VMP-3 electrochemical workstation (Biologic Science, France). For oxidation stability of the electrolytes, a CR2032 type coin cell was assembled with lithium (Li) foil (diameter = 15.6 mm, thickness = 0.45 mm, TMAX Ltd., Xiamen, China) as the CE and the RE, and an Al foil (diameter = 16 mm, Cambridge Energy Solution, UK) as the WE. A Whatman glass fiber (diameter = 20 mm, Whatman, Grade GF/A) used as a separator and ~150  $\mu\text{L}$  of the electrolyte was added. The LSV scans on Al substrate were performed from OCV to 5.5 V vs. Li/Li<sup>+</sup> at a scanning rate of 1  $\text{mV s}^{-1}$ . For CA experiments, 3.9 V and 5.0 V vs. Li/Li<sup>+</sup> was applied to the cell for 6 h to evaluate Al passivation.

A Li symmetric cell configuration with a 2032 type coin cell was used for Li plating-striping experiments and polarization time of 1 h was employed for plating and stripping. Rate performance of the Li symmetric cells was tested using current densities of 0.05, 0.1, 0.2, and 0.1  $\text{mA cm}^{-2}$  consecutively, and the long-term performance was evaluated with a constant current of 0.1  $\text{mA cm}^{-2}$  Li metals as both anode and cathode (diameter = 15.6 mm, thickness = 0.45 mm, TMAX Ltd., Xiamen, China), and a Whatman glass fiber (diameter = 20 mm, Whatman, Grade GF/A) was used as a separator, with ~150  $\mu\text{L}$  of electrolyte. At least two cells were fabricated and tested for each electrolyte and the experiments were carried out at least 12 h after the cells were coined.

## Viscosity

The viscosities of the electrolytes were measured using an Anton Paar SmartPave 92 rheometer, with a plate-plate configuration (20-mm diameter, 1-mm gap). The shear stress and viscosity were tested by shear rates ranging from 1 to 100 (1/s) at a temperature range from 20 to 100 °C.

## Scanning Electron Microscopy

The morphology of the crystals as well as the electrodes before and after electrochemical tests was assessed by a scanning electron

microscope (SEM, FEI Magellan 400 field emission XHR-SEM) operated at an accelerating voltage of 3 kV and working distance of ~5.4 mm. A conductive carbon tape was stuck onto the sample holder and the sample applied to the tape.

## Results and Discussion

Here, we start with describing the crystal structures of the LiBGB and NaBGB salts as well as assessment of their stability vs. moisture, followed by thermal stability and phase behavior studies of all the salts. Subsequently, systematic investigations of the transport properties including viscosity, ionic conductivity, and ion diffusion of the LiBGB-based electrolytes are emphasized. Finally, the electrochemical properties, Al passivation effect and Li metal compatibility are explored and discussed in detail.

## Crystal Structures and Stability vs. Moisture

The LiBGB and NaBGB salts displayed cuboid-shape and rod-shape structures, respectively, as observed by SEM (Figure S18). These regular but different morphologies arose our interest, why we decided to attempt to obtain single crystals to gain further insight into their structure. Figure 2 shows the asymmetric unit of LiBGB·H<sub>2</sub>O and NaBGB·2H<sub>2</sub>O crystallized in the monoclinic space groups P21/c and P21/n, respectively. Table S2 summarizes the pertinent crystallographic data and Table S3 presents the bond lengths in the structures of LiBGB·H<sub>2</sub>O and NaBGB·2H<sub>2</sub>O. The coordination environment about the lithium center includes two intracyclic oxygen atoms of the two BGB anions, one exocyclic oxygen of the BGB anion, and one molecule of water (Figure S19a). Such a tetra-coordinated lithium serves to form two-dimensional sheets in the ac crystal plane and furthermore polymeric sheets are extended in three dimensions through hydrogen bonds (Figure S19b). Similar to the hydrates of BGB salts, alkali metal salts of BOB anions are known to crystalize in the form of solvates from the solvent that is used for crystallization.<sup>[19,20]</sup> Zavalij *et al.* have reported crystal data of both anhydrous LiBOB<sup>[19]</sup> and LiBOB·H<sub>2</sub>O,<sup>[20]</sup> and the BOB anion behaved in a similar way. The

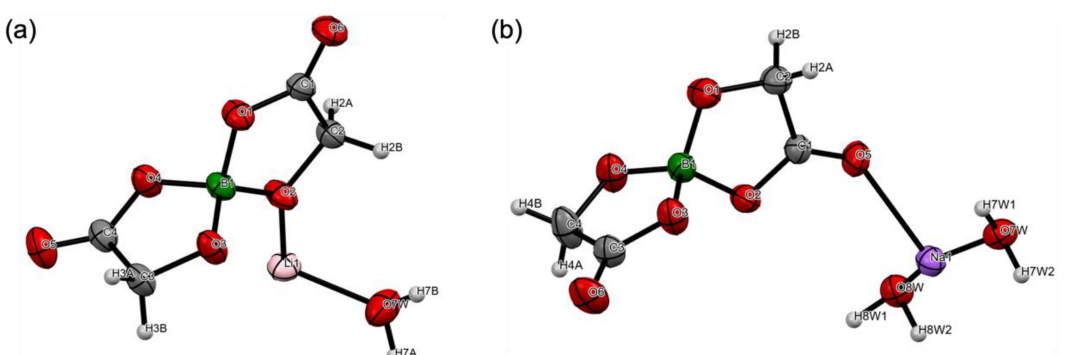


**Figure 2.** Thermal ellipsoid plots of a symmetric unit contained in the crystal structures of (a) LiBGB·H<sub>2</sub>O and (b) NaBGB·2H<sub>2</sub>O. Ellipsoids are shown at the 50% probability level with atom labeling scheme.

Li atom in BOB salts has octahedral coordination in the solvates, achieved by at least one solvent molecule needed to be coordinated which can be attributed to the rigid nature of the BOB anion.<sup>[20]</sup>

Unlike the LiBGB salt, the arrangement adopted by NaBGB·2H<sub>2</sub>O differs as the sodium center is coordinated to two exocyclic oxygen atoms of the two BGB anions and two discrete water molecules, alongside two water molecules bridging two sodium centers, and this way forming hexa-coordinated sodium centers (Figure S20a). The crystal structure packing of NaBGB·2H<sub>2</sub>O looking down the a-axis shows the corrugated polymeric network in three dimensions (Figure S20b).

While LiBOB and NaBOB salts suffer from moisture instability, in particular LiBOB is proven to decompose and produce B(C<sub>2</sub>O<sub>4</sub>)(OH) and LiB(C<sub>2</sub>O<sub>4</sub>)(OH)<sub>2</sub> - compounds that can significantly impair battery performance,<sup>[23,35]</sup> LiBGB and NaBGB exhibit exceptional stability vs. moisture (Figures 3a and b, S1–S8 and S22–S29) as any structural cleavage of the anion would have been detected, especially by the <sup>11</sup>B NMR spectroscopy due to its sensitivity to structural changes.<sup>[45]</sup> The minor shifts in the <sup>7</sup>Li and <sup>23</sup>Na NMR resonance lines of LiBGB and NaBGB (Figures S42 and S43) are likely explained by interactions with water molecules, as is also confirmed by the single crystal structures (Figure 2).

The main reason for this stability vs. moisture is the stronger complexation propensity of the alpha-hydroxycarboxylic acid to boron as compared with the dicarboxylic acid, primarily attributed to electronic effects and ring strains.<sup>[46]</sup> Additionally,

this stability vs. moisture is also transferred to the electrolytes (Figures S30–S41); Chemical shifts of <sup>11</sup>B and <sup>1</sup>H NMR spectra for fresh and air-exposure electrolytes remain almost unchanged and no additional resonance lines appear (Figures 3c and d, S30–S41), indicating that the humid air has no influence on the chemical structure of the BGB anion. Again, the minor shifts in the <sup>7</sup>Li and <sup>23</sup>Na NMR resonance lines can be attributed to interactions with water molecules (Figure S43). Overall, the results confirm superior stability vs. moisture for BGB-based salts and LiBGB-based electrolytes.

### Thermal Stabilities and Phase Transitions

Assessing thermal stability of electrolyte salts is of great importance for battery applications and thus thermal gravimetric analysis (TGA) and differential thermogravimetry (DTG) are employed to investigate the thermal behavior of the BGB-based salts (Figure 4). The nature and size of the inorganic cation play a crucial role in the thermal behavior of these BGB-based salts (Figure 4a). The Li-salt has the highest  $T_{decomp}$  370 °C, while the Ca-salt has the lowest, and the overall trend of decomposition temperature follows the sequence of: Li > Na > K > Mg > Ca (Table S4). For both mono- and divalent cations, the ionic interactions decrease with increasing ionic radius at the same group, thus exhibiting lower  $T_{decomp}$  for the salts with larger cations. The lower thermal stabilities of the salts with divalent cations are probably due to the presence of two BGB anions

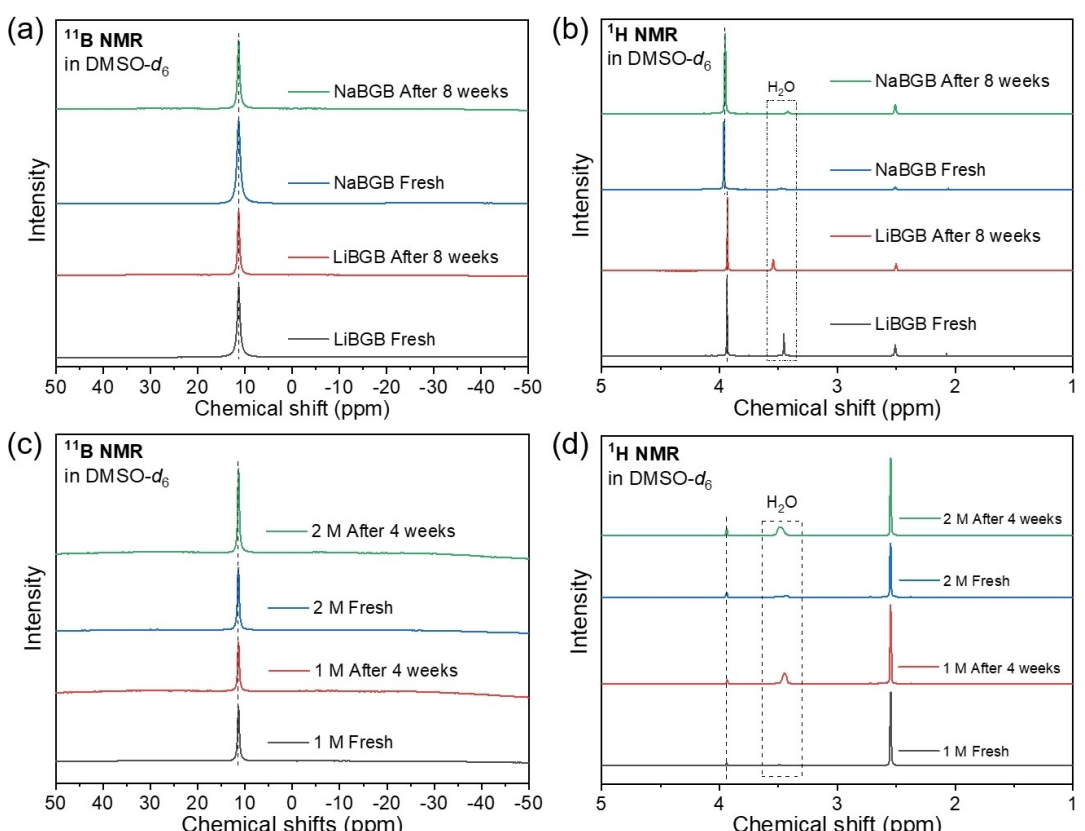
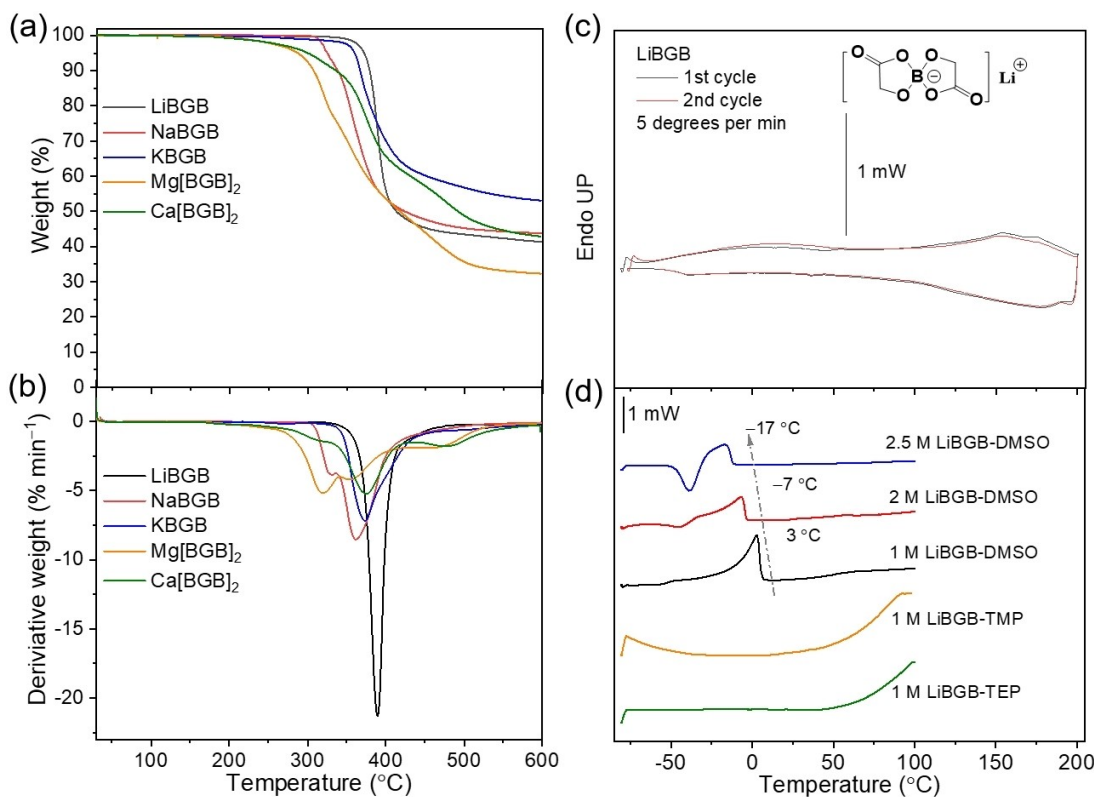


Figure 3. (a, c) <sup>11</sup>B NMR and (b, d) <sup>1</sup>H NMR spectra of the salts and the electrolytes in DMSO before and after exposure to moisture.



**Figure 4.** (a) TGA and (b) DTG curves of the BGB-based salts, and DSC traces of (c) LiBGB, and (d) LiBGB-based electrolytes.

and thus existence of larger organic contents than the salts of monovalent cations. Since  $Mg^{2+}$  is smaller and more electro-negative than  $Ca^{2+}$ ,<sup>[47]</sup> it presents stronger coulombic interactions with the BGB anions and therefore  $Mg[BGB]_2$  is thermally more stable than  $Ca[BGB]_2$ . Compared to the structural analogous LiBOB and NaBOB, which decompose at 302 °C<sup>[48]</sup> and 300 °C,<sup>[12]</sup> respectively, the BGB-based Li and Na salts exhibit much higher thermal stabilities (375 °C and 330 °C, respectively). Excepted LiBGB, all the salts present several decomposition steps, where the rate of weight loss varies for each decomposition step (Figure 4b); the Li-salt has the highest rate of  $> 20\% \text{ min}^{-1}$  in a single-step around 370 °C, while all the other salts have  $< 10\% \text{ min}^{-1}$ . The Na- and K-salts present weight loss in two steps, while the Mg- and Ca-salts in three steps. In contrast to LiBOB, which has a two-step thermal decomposition process,<sup>[21]</sup> the LiBGB decomposes in a single step at a much higher temperature. For the divalent salts, the situation is more complicated since these salts contain two BGB anions; the larger organic contents decrease the overall thermal decomposition temperatures as well as is associated with multistep decomposition process. The multistep decompositions point towards formation of solid decomposition products that decompose at higher temperatures and thus weight loss occur at different temperatures.

There are no visible phase transitions from -175 to 200 °C, excepted NaBGB with a phase transition at ca. 100 °C in the first heating scan only (Figures 4c and S44). For the electrolytes, no phase transitions are observed for 1 M LiBGB in TMP or TEP

from -75 to 50 °C (Figure 4d). However, the electrolytes based on DMSO present glass transition temperatures, which are clearly affected by the salt concentration and the anti-freezing capability is improved down to -17 °C by increasing the salt concentration up to 2.5 M. Additionally, the electrolytes exhibit a typical supercooling ability at salt concentrations  $> 1\text{ M}$ ,<sup>[49]</sup> which is confirmed by storing the 2 M and 2.5 M LiBGB in DMSO electrolytes at -23 °C for 15 h, and these remained liquid (Figure S45).

#### Ion Transport and Ionic Interactions

Fast ion transport/high ionic conductivity is essential to allow for fast battery charging<sup>[50,51]</sup> and for the LiBGB electrolytes this is strongly influenced both by the nature of the solvent as well as the salt concentration (Figure 5a). The decreased ionic conductivity with increasing salt concentration is associated with ion-pair and/or aggregate formation, reducing the number of effective charge carriers, as well as increased viscosity.<sup>[52]</sup> Notably, the viscosity of the 2.5 M LiBGB-DMSO electrolyte is ca. 6 and 2 times higher than the 1 and 2 M concentrated electrolytes (Figure 5b), but at the same time its ionic conductivity is comparable to the 1 M LiBGB-TMP electrolyte, showing the large role of the solvent employed. For the same salt concentration, 1 M, the viscosities of LiBGB-TEP, LiBGB-TMP and LiBGB-DMSO are quite comparable, but the latter exhibits much higher ionic conductivities (above 10 °C) and with

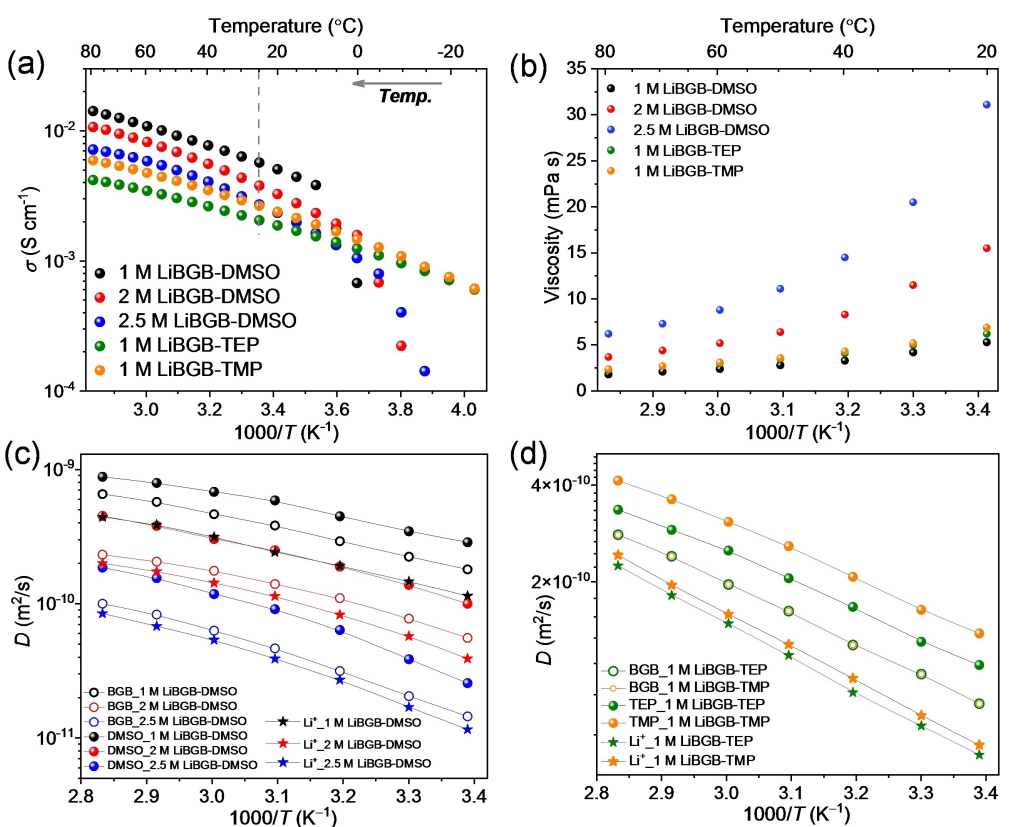


Figure 5. (a) Ionic conductivity, (b) viscosity, and (c, d) diffusion coefficients of the LiBGB-based electrolytes.

5.7 mS cm $^{-1}$  at 25 °C it is only slightly less than conductive than our benchmark 1 M LiPF $_6$  in EC-DEC electrolyte (7.6 mS cm $^{-1}$ )<sup>[53]</sup> (Table S5).

Independent of the nature of the organic solvent it always diffuses the fastest, followed by the BGB anion and the Li $^{+}$  cation being the slowest (Figure 5c and d) and furthermore, at a comparable 1 M concentration, it follows their molecular sizes: DMSO > TMP > TEP; Diffusion coefficients of Li $^{+}$  ( $D_{\text{Li}^+}$ ) and BGB anion ( $D_{\text{BGB}}$ ) for 1 M LiBGB-DMSO are almost 1.5 times and ~2.3 times higher than LiBGB-TMP and LiBGB-TEP at the given temperature range (Figures 5c and d), while the difference of  $D_{\text{Li}^+}$  and  $D_{\text{BGB}}$  in LiBGB-TMP and LiBGB-TEP is very minor (Figure 5d). Upon increased LiBGB concentration all diffusivities decrease, which follow from increased viscosity and ion-pairing/aggregation, as outlined above. As compared to the reported orthoborate-based electrolytes, the ionic conductivity of 1 M LiBGB-DMSO electrolyte is slightly higher than for both 1 M lithium bis(malonato)borate (LiBMLB) and lithium bis(fluoromalonato)borate (LiBFMB) in DMSO (5.7 vs. ~5.4 and ~5.3 mS cm $^{-1}$ ),<sup>[54]</sup> while slightly lower than for 1 M LiBOB in DMSO (5.7 vs. ~7.0 mS cm $^{-1}$ ).<sup>[54]</sup> The trend of ion conductivity could be attributed to the influence of viscosity, i.e. ~5.0 for LiBGB vs. 4.7, 6.1 and 6.1 mPa s for LiBOB, LiBMLB and LiBFMB, respectively at 25 °C.<sup>[54]</sup> A summary of the above-mentioned properties is presented in Table S6 to compare with Li-salts comprising other orthoborate anions including BOB, BMLB and BFMB. From this, the BGB anion is found to offer superior

thermal stability together with excellent moisture stability, while the  $D_{\text{Li}^+}$  and  $D_{\text{BGB}}$  for LiBGB are 36% and 14%, and 36% and 22% lower than for LiBMLB and LiBFMB in DMSO, respectively.

The ion-solvent interactions are probed using first a “dilute” LiBGB in DMSO-*d*6, which shows a narrow and single  $^7\text{Li}$  NMR resonance line (Figure S4), and then by all the electrolytes have unsymmetric shapes and line splits (Figure 6a), clearly suggesting the formation of various solvates. In particular, there is a ~0.5 ppm up-field shift for the 2 M and 2.5 M LiBGB-DMSO electrolytes, from the 1 M LiBGB-DMSO, indicating a gradual strengthening of the ion-solvent-ion association.<sup>[55,56]</sup> In addition, unlike the relatively sharp  $^7\text{Li}$  NMR resonance lines (< 15 Hz) of the DMSO-based electrolytes, the resonance lines of TMP- and TEP-based electrolytes are much broader (> 50 Hz) pointing to different modes of interactions of these solvents and also the BGB anion with the Li $^{+}$  cation (Table S7). The larger up-field shift of the TEP-based electrolyte indicates stronger interaction of TEP with Li $^{+}$  as compared to with TMP and DMSO (at the same 1 M salt concentration),<sup>[56]</sup> again in accordance with the ionic conductivity data.

Moving to the  $^{11}\text{B}$  NMR resonance lines these are shifting up-field with increasing salt concentration for the DMSO-based electrolytes, suggesting aggregate formation due to strong Li $^{+}$ -BGB interactions,<sup>[57]</sup> while the linewidths increase significantly, from 99 Hz to 416 Hz (Table S7), indicating less re-orientational mobility of the anion, induced by the increased viscosity and

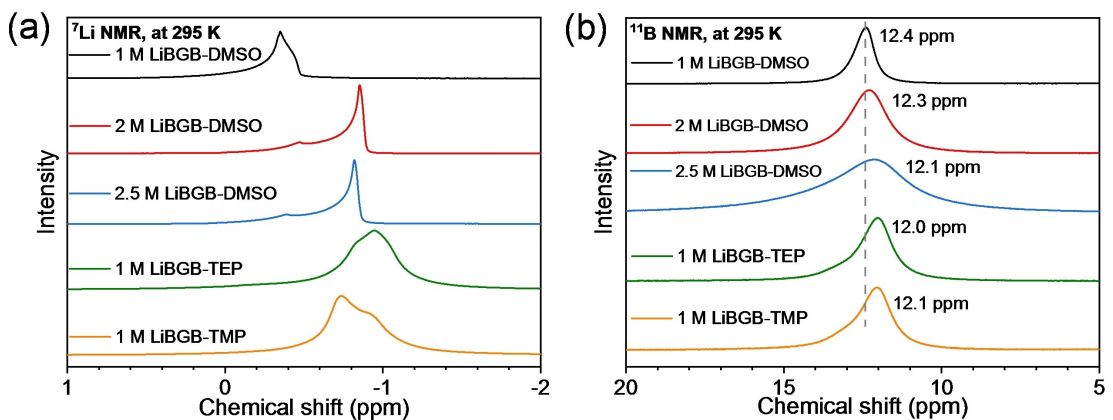


**Figure 6.** (a)  $^{7}\text{Li}$  NMR, and (b)  $^{11}\text{B}$  NMR spectra of the LiBGB-based electrolytes at 295 K.

cation interactions. For a common 1 M salt concentration, the LiBGB-TEP and LiBGB-TMP electrolytes both exhibit broader linewidths and larger up-field shifts as compared to the LiBGB-DMSO electrolyte (Figure 6b and Table S7), which is consistent with the  $^{7}\text{Li}$  NMR spectra. Once again, this agrees well with reduced mobility of BGB, by aggregation, including the differences in diffusivity of TEP and TMP as compared to DMSO despite the comparable viscosities of the pure solvents.

### Electrochemical Stability

The electrochemical stability of the 1 M LiBGB-DMSO electrolyte using GC as the WE shows a wide electrochemical stability window (ESW) (Figure 7a), with an oxidation peak at  $\sim 4.6$  V vs.  $\text{Li}/\text{Li}^+$ , but higher salt concentrations widen the ESWs: 5.50 and 5.87 V for the 2 M and 2.5 M electrolytes, respectively. This is in accordance with other lithium and sodium battery electrolytes, based on the fluorine-containing non-orthoborate anion.<sup>[58-61]</sup> Overall, the LiBGB-TEP and LiBGB-TMP electrolytes display even better reduction stabilities, the latter having the widest ESW (6.11 V) (Table S8).

Furthermore, the 1 M LiBGB-DMSO does not passivate the Al surface properly, why there is an oxidation peak at  $\sim 3.5$  V vs.  $\text{Li}/\text{Li}^+$  (Figure S46a), but again this is improved with increasing salt concentration – resulting in a very rapid increase in current density at  $\sim 4.5$  V vs.  $\text{Li}/\text{Li}^+$  (Figure 7b), most probably due to the oxidation of DMSO as reported on by Kwabi *et al.*<sup>[62]</sup> Both the TEP- and TMP-based electrolytes display much lower current density up to 5 V vs.  $\text{Li}/\text{Li}^+$  on Al WE, indicating much better oxidation stabilities, and the former clearly surpasses beyond the benchmark electrolyte at the given potential range (Figure 7b).

### Passivation of Aluminum

Using the 1 M LiBGB-DMSO electrolyte there is a much higher polarization current at 3.9 V vs.  $\text{Li}/\text{Li}^+$  than other electrolytes and the impedance increase is accompanied with distorted signals (Figures 8a and S46b). Further, the 1 M LiBGB-TEP electrolyte presents a higher polarization current than 1 M LiBGB-TMP, which shows almost the same polarization as 1 M  $\text{LiPF}_6$ /EC-DEC. The polarization is suppressed with increasing

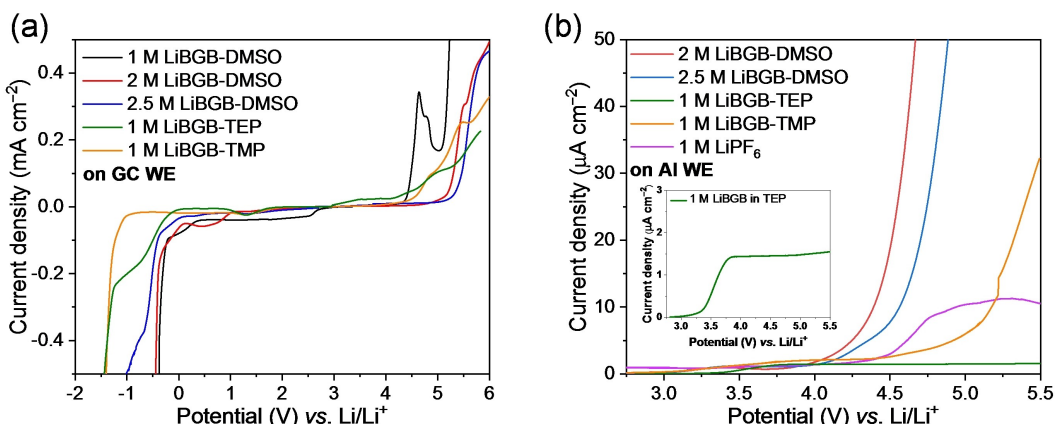


**Figure 7.** LSV of LiBGB-based electrolytes (a) on GC electrode, and (b) on Al substrate in comparison with 1 M  $\text{LiPF}_6$  in EC-DEC electrolyte.

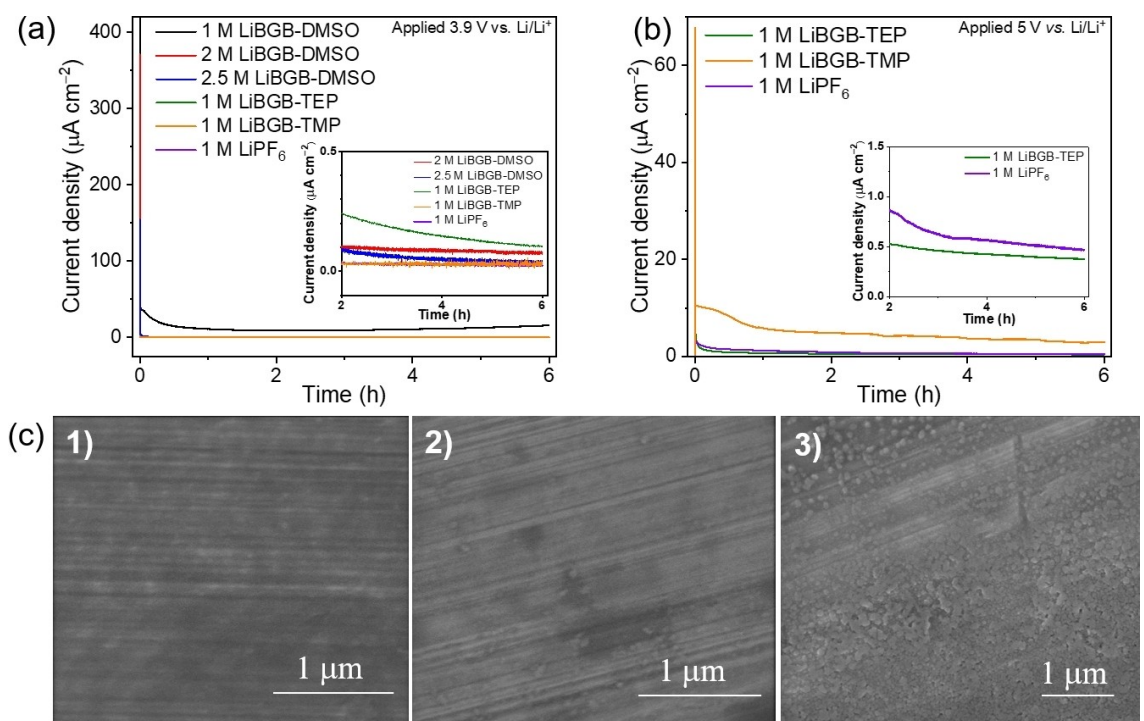


**Figure 8.** CA profiles at potentials of: (a) 3.9 V vs. Li/Li<sup>+</sup> and (b) 5 V vs. Li/Li<sup>+</sup> and (c) the SEM images of the Al substrate: (1) fresh and post-CA (5 V vs. Li/Li<sup>+</sup>) with the (2) 1 M LiBGB-TEP and (3) benchmark LP40 electrolytes.

salt concentration; the polarization current for the 2.5 M LiBGB-DMSO electrolyte is slightly lower than for the 2 M electrolyte.

Based on the overall electrochemical stability, the 1 M LiBGB-TEP, 1 M LiBGB-TMP and benchmark LP40 electrolytes were selected for further evaluation at a higher voltage of 5 V vs. Li/Li<sup>+</sup> (Figure 8b). Here the 1 M LiBGB-TEP achieves a much lower current density than the 1 M LiBGB-TMP electrolyte does, as well as a slightly smaller current density than the benchmark electrolyte. The post-CA morphologies of the Al surfaces (Figure 8c) show that the 1 M LiBGB-TEP electrolyte has not caused any changes overall, while the benchmark electrolyte renders white pits and increased roughness. It is thus clear that the fluorine-free 1 M LiBGB-TEP electrolyte can passivate the Al substrate at this high potential.

### Electrochemical Assessment of Li Symmetrical Cells

The lithium metal plating-stripping tests using symmetrical Li||Li cells subjected to different current densities (Figures 9a and S47) first of all show that, due to the poor stability of DMSO towards Li metal,<sup>[63,64]</sup> the 1 M LiBGB-DMSO electrolyte based cell becomes short circuit after 60 h, when the current density was changed from 0.2 mA cm<sup>-2</sup> to 0.1 mA cm<sup>-2</sup> and in addition a much higher impedance is observed after cycling due to the cell failure (Figures S47 and S48a). In contrast, the cell using the 2 M LiBGB-DMSO electrolyte performs much better, which might be attributed to the higher salt content of this electrolyte. However, when the concentration is further increased to 2.5 M LiBGB-DMSO electrolyte, the plating-stripping process is

less reversible, likely due to the higher viscosity and lower ionic conductivity (Figures S47 and S48c). Hence, there is an optimal salt concentration balancing the reactivity and ion transport properties.

In comparison, the 1 M LiBGB-TMP electrolyte-based cell has larger overpotentials than the 2 M LiBGB-DMSO electrolyte based one (Figure 9a), but the evolution of their voltage profiles differ (Figures 9b–e), probably influenced by the transport properties. The overpotentials of both fluorine-free and fluorinated ones are lower at the initial cycles (Figure 9b), suggesting the formation of a favorable surface layer and the increased active surface area.<sup>[65]</sup> Afterwards the overall cell polarization for each electrolyte is increased, but is obviously more serious for the fluorine-free electrolytes, which might be attributed to the “dead” lithium.<sup>[65]</sup> The 1 M LiBGB-TMP presents a similar “arching” voltage profile as the benchmark electrolyte compared to the “peaking” voltage profile for 2 M LiBGB-DMSO with increased current densities while the benchmark electrolyte shows much smaller overpotentials with minor changes (Figure 9c–e). The “peaking” voltage profile for 2 M LiBGB in DMSO is most probably due to unfavorable reactions between the Li metal surface and the high polarity and aggressive DMSO solvent, whereby the Li metal may form oxides and/or hydroxides. However, the 1 M LiBGB-TEP electrolyte undergoes enormously increased overpotentials with higher impedance after cycling, implying a poor Li compatibility (Figures S47 and S48d).

Subsequently, a comparison of the long-term Li||Li symmetrical cell polarization profiles of 2 M LiBGB-DMSO, 1 M LiBGB-TMP, and the benchmark electrolyte at 0.1 mA cm<sup>-2</sup> for

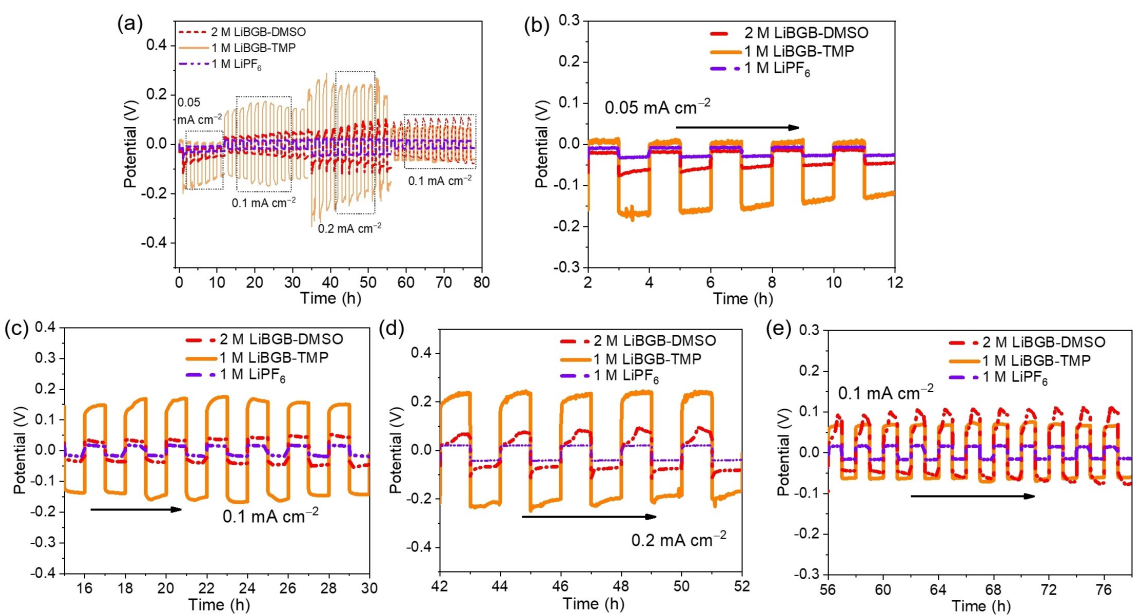


**Figure 9.** (a) Li||Li symmetrical cell polarization profiles for different electrolytes at various current densities, (b–e) Zoom-in polarization profiles at different time intervals.

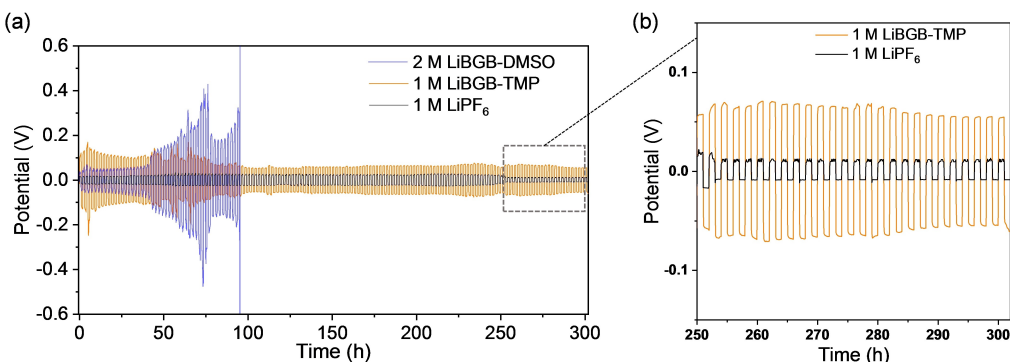


**Figure 10.** (a, b) Long-term Li||Li symmetrical cell polarization profiles of the three selected electrolytes.

300 h is investigated (Figure 10a). The 1 M LiBGB-TMP electrolyte displays superior long-term stability compared to the 2 M LiBGB-DMSO even though it suffers from higher overpotentials at the first 50 h. The decrease in overpotential after 50 h for the 1 M LiBGB-TMP based cell is probably due to the formation of a robust interface and furthermore the overpotential also remains stable until at least 300 h while admittedly the cell performance of the benchmark electrolyte is much better than 1 M LiBGB-TMP in terms of overpotential and cell impedance, but the results are still more or less evident that BGB-based electrolyte can stabilize the surface of lithium metal (Figure 10b). Altogether, the 1 M LiBGB-TMP electrolyte provides a new and broad possibility for designing fluorine-free electrolytes, not limited to LIBs but other battery technologies as well.

## Conclusions

The new fluorine-free orthoborate-based salts and the corresponding DMSO, TEP and TMP electrolytes have promising transport properties, high moisture stability and ample Al passivation as well as Li metal compatibility. The BGB anion also outperforms the analogous BOB anion in terms of thermal and moisture stabilities. Using a slightly higher salt concentration (2 M rather than 1 M) partially suppresses the instability of the DMSO solvent, putting forward the use of this solvent in electrolytes. The 1 M LiBGB-TMP electrolyte demonstrates the best performance not only in terms of transport properties but also in terms Al passivation and Li plating-stripping, suggesting this to be an alternative to fluorinated electrolytes. Overall, the BGB-based salts and electrolytes have a great potential to be further optimized using different solvents and additives, providing a new route to hydrolytically stable fluorine-free electrolytes for both mono- and divalent rechargeable batteries.

## Acknowledgements

The authors gratefully acknowledge financial supports from the Swedish Research Council for Sustainable Development (Grant number: 2020-00969). P.J. is also grateful for the financial support from his Swedish Research Council (VR) Distinguished Professor grant 'Next Generation Batteries' (#2021-00613). M.R.S. gratefully acknowledge the financial support from the Knut and Alice Wallenberg Foundation (Grant number: 2019.0124). The authors thank Ms. Marieke Verberne for assistance in moisture stability experiments.

## Conflict of Interests

The authors declare no conflict of interest.

## Data Availability Statement

The data that support the findings of this study are available from the corresponding author upon reasonable request.

**Keywords:** Borate salts • Fluorine-free electrolytes • Electrochemical assessments • Transport properties • Li compatibility

- [1] Y. Zhao, J. Zhang, Y. Xie, B. Sun, J. Jiang, W.-J. Jiang, S. Xi, H. Y. Yang, K. Yan, S. Wang, X. Guo, P. Li, Z. Han, X. Lu, H. Liu, G. Wang, *Nano Lett.* **2021**, *21*, 823–832.
- [2] G. Severa, E. Rönnebro, C. M. Jensen, *Chem. Commun.* **2010**, *46*, 421–423.
- [3] D. Zhao, Y. Wang, C.-L. Dong, Y.-C. Huang, J. Chen, F. Xue, S. Shen, L. Guo, *Nat. Energy* **2021**, *6*, 388–397.
- [4] K. Xu, S. Zhang, T. R. Jow, W. Xu, C. A. Angell, *Electrochim. Solid-State Lett.* **2001**, *5*, A26.
- [5] A. Du, Z. Zhang, H. Qu, Z. Cui, L. Qiao, L. Wang, J. Chai, T. Lu, S. Dong, T. Dong, H. Xu, X. Zhou, G. Cui, *Energy Environ. Sci.* **2017**, *10*, 2616–2625.
- [6] M. Hong, S. Lee, V.-C. Ho, D. Lee, S.-H. Yu, J. Mun, *ACS Appl. Mater. Interfaces* **2022**, *14*, 10267–10276.
- [7] L. O. S. Colbin, R. Mogensen, A. Buckel, Y.-L. Wang, A. J. Naylor, J. Kullgren, R. Younesi, *Adv. Mater. Interfaces* **2021**, *8*, 2101135.
- [8] S. S. Zhang, K. Xu, T. R. Jow, *J. Electrochem. Soc.* **2002**, *149*, A586.
- [9] B. S. Parimalam, B. L. Lucht, *J. Electrochim. Soc.* **2018**, *165*, A251.
- [10] X. Yi, X. Li, J. Zhong, Z. Cui, Z. Wang, H. Guo, J. Wang, G. Yan, *ACS Appl. Mater. Interfaces* **2024**, *16*, 11585–11594.
- [11] W. Xu, C. A. Angell, *Electrochim. Solid State Lett.* **2001**, *4*, L3.
- [12] R. Mogensen, S. Colbin, A. S. Menon, E. Björklund, R. Younesi, *ACS Appl. Energy Mater.* **2020**, *3*, 4974–4982.
- [13] Y. Wang, S. Ma, H. Wang, *ChemSusChem* **2023**, *16*, e202201218.
- [14] L. Gao, J. Chen, Q. Chen, X. Kong, *Sci. Adv.* **2022**, *8*, eabm4606.
- [15] Z. Liu, W. Hou, H. Tian, Q. Qiu, I. Ullah, S. Qiu, W. Sun, Q. Yu, J. Yuan, L. Xia, X. Wu, *Angew. Chem. Int. Ed.* **2024**, *63*, e202400110.
- [16] S. Li, Q. Liu, W. Zhang, L. Fan, X. Wang, X. Wang, Z. Shen, X. Zang, Y. Zhao, F. Ma, Y. Lu, *Adv. Sci. (Weinh.)* **2021**, *8*, 2003240.
- [17] B. Roy, P. Cherepanov, C. Nguyen, C. Forsyth, U. Pal, T. C. Mendes, P. Howlett, M. Forsyth, D. MacFarlane, M. Kar, *Adv. Energy Mater.* **2021**, *11*, 2101422.
- [18] R. Mogensen, A. Buckel, S. Colbin, R. Younesi, *Chem. Mater.* **2021**, *33*, 1130–1139.
- [19] P. Y. Zavalij, S. Yang, M. S. Whittingham, *Acta Crystallograph. Section B* **2003**, *59*, 753–759.
- [20] P. Y. Zavalij, S. Yang, M. S. Whittingham, *Acta Crystallograph. Sect. B* **2004**, *60*, 716–724.
- [21] E. Zinigrad, L. Larush-Asraf, G. Salitra, M. Sprecher, D. Aurbach, *Thermochim. Acta* **2007**, *457*, 64–69.
- [22] J. Guzmán-Torres, D. L. Ochoa-Gamboa, L. L. Garza-Tovar, L. C. Torres-González, S. M. de la Parra-Arciniega, E. González-Juárez, I. Gómez, E. M. Sánchez, *J. Electron. Mater.* **2023**, *52*, 1250–1257.
- [23] L. Yang, M. M. Furczon, A. Xiao, B. L. Lucht, Z. Zhang, D. P. Abraham, *J. Power Sources* **2010**, *195*, 1698–1705.
- [24] X. Min, C. Han, S. Zhang, J. Ma, N. Hu, J. Li, X. Du, B. Xie, H.-J. Lin, C.-Y. Kuo, C.-T. Chen, Z. Hu, L. Qiao, Z. Cui, G. Xu, G. Cui, *Angew. Chem. Int. Ed.* **2023**, *62*, e202302664.
- [25] J. Forero-Saboya, C. Davoisne, R. Dedryvère, I. Yousef, P. Canepa, A. Ponrouch, *Energy Environ. Sci.* **2020**, *13*, 3423–3431.
- [26] N. T. Hahn, J. Self, K. S. Han, V. Murugesan, K. T. Mueller, K. A. Persson, K. R. Zavadil, *J. Phys. Chem. B* **2021**, *125*, 3644–3652.
- [27] T. S. Arthur, P.-A. Glans, N. Singh, O. Tutusaus, K. Nie, Y.-S. Liu, F. Mizuno, J. Guo, D. H. Alsem, N. J. Salmon, R. Mohrtadi, *Chem. Mater.* **2017**, *29*, 7183–7188.
- [28] Z. Zhao-Karger, M. E. Gil Bardaji, O. Fuhr, M. Fichtner, *J. Mater. Chem. A* **2017**, *5*, 10815–10820.
- [29] A. Shyamsunder, L. E. Blanc, A. Assoud, L. F. Nazar, *ACS Energy Lett.* **2019**, *4*, 2271–2276.
- [30] G. Hernández, R. Mogensen, R. Younesi, J. Mindemark, *Batteries & Supercaps* **2022**, *5*, e202100373.
- [31] A. Ponrouch, A. R. Goñi, M. R. Palacín, *Electrochim. Commun.* **2013**, *27*, 85–88.
- [32] A. Downard, M. Nieuwenhuyzen, K. R. Seddon, J.-A. van den Berg, M. A. Schmidt, J. F. S. Vaughan, U. Welz-Biermann, *Crystal Growth Design* **2002**, *2*, 111–119.
- [33] P. Johansson, *Phys. Chem. Chem. Phys.* **2007**, *9*, 1493–1498.
- [34] P. Jankowski, W. Wieczorek, P. Johansson, *Phys. Chem. Chem. Phys.* **2016**, *18*, 16274–16280.
- [35] C. Li, Z. Li, P. Wang, H. Liu, D. Zhao, S. Wang, S. Li, *New J. Chem.* **2019**, *43*, 14238–14245.
- [36] J. Barthel, M. Wühr, R. Buestrich, H. J. Gores, *J. Electrochim. Soc.* **1995**, *142*, 2527.
- [37] J. Barthel, R. Buestrich, E. Carl, H. J. Gores, *J. Electrochim. Soc.* **1996**, *143*, 3572.
- [38] J. Barthel, R. Buestrich, H. J. Gores, M. Schmidt, M. Wühr, *J. Electrochim. Soc.* **1997**, *144*, 3866.
- [39] P. T. Anastas, J. C. Warner, *Green Chemistry: Theory and Practice*, Oxford University Press **1998**.
- [40] B. Akesson, *International Programme on Chemical, S-, N-methyl-2-pyrrolidone*. World Health Organization: Geneva, 2001.
- [41] J. Sherwood, T. J. Farmer, J. H. Clark, *Chem* **2018**, *4*, 2010–2012.
- [42] C. B. Hübschle, G. M. Sheldrick, B. Dittrich, *J. Appl. Crystallogr.* **2011**, *44*, 1281–1284.
- [43] Diamond – Crystal and Molecular Structure Visualization, Crystal Impact – Dr. H. Putz, Dr. K. Brandenburg GbR, Kreuzherrenstr. 102, 53227 Bonn, Germany (Please see: <https://www.crystalimpact.de/diamond>).
- [44] R. Wibowo, L. Aldous, S. E. Ward Jones, R. G. Compton, *ECS Trans.* **2019**, *33*, 523–535.
- [45] A. Filippov, O. N. Antzutkin, F. U. Shah, *ACS Sustain. Chem. Eng.* **2020**, *8*, 552–560.
- [46] M. Van Duin, J. A. Peters, A. P. G. Kieboom, H. Van Bekkum, *Tetrahedron* **1984**, *40*, 2901–2911.
- [47] K. Li, D. Xue, *J. Phys. Chem. A* **2006**, *110*, 11332–11337.
- [48] W. Xu, C. A. Angell, *Electrochim. Solid-State Lett.* **2001**, *4*, E1.
- [49] Z. Wojnarowska, S. Cheng, B. Yao, M. Swadzba-Kwasny, S. McLaughlin, A. McGrogan, Y. Delavoux, M. Paluch, *Nat. Commun.* **2022**, *13*, 1342.
- [50] E. R. Logan, J. R. Dahn, *Trends Chem.* **2020**, *2*, 354–366.
- [51] Y. Liu, Y. Zhu, Y. Cui, *Nat. Energy* **2019**, *4*, 540–550.
- [52] V. Nilsson, D. Bernin, D. Brandell, K. Edström, P. Johansson, *ChemPhysChem* **2020**, *21*, 1166–1176.
- [53] P. Murmann, R. Schmitz, S. Nowak, H. Gores, N. Ignatiev, P. Sartori, S. Passerini, M. Winter, R. W. Schmitz, *J. Electrochim. Soc.* **2013**, *160*, A535.
- [54] C. Liao, K. S. Han, L. Baggetto, D. A. Hillesheim, R. Custelcean, E.-S. Lee, B. Guo, Z. Bi, D.-E. Jiang, G. M. Veith, E. W. Hagaman, G. M. Brown, C. Bridges, M. P. Paranthaman, A. Manthiram, S. Dai, X.-G. Sun, *Adv. Energy Mater.* **2014**, *4*, 1301368.
- [55] I. Ruggeri, *ChemElectroChem* **2019**, *6*, 4002–4009.
- [56] Z. Jiang, Z. Zeng, X. Liang, L. Yang, W. Hu, C. Zhang, Z. Han, J. Feng, J. Xie, *Adv. Funct. Mater.* **2021**, *31*, 2005991.
- [57] J. Peng, M. Gobet, M. Devany, K. Xu, A. W. Cresce, O. Borodin, S. Greenbaum, *J. Power Sources* **2018**, *399*, 215–222.

- [58] J. Lee, Y. Lee, J. Lee, S.-M. Lee, J.-H. Choi, H. Kim, M.-S. Kwon, K. Kang, K. T. Lee, N.-S. Choi, *ACS Appl. Mater. Interfaces* **2017**, *9*, 3723–3732.
- [59] L. Suo, W. Xue, M. Gobet, S. G. Greenbaum, C. Wang, Y. Chen, W. Yang, Y. Li, J. Li, *Proc. Natl. Acad. Sci.* **2018**, *115*, 1156–1161.
- [60] K. Yoshida, M. Nakamura, Y. Kazue, N. Tachikawa, S. Tsuzuki, S. Seki, K. Dokko, M. Watanabe, *J. Am. Chem. Soc.* **2011**, *133*, 13121–13129.
- [61] Y. Yamada, K. Furukawa, K. Sodeyama, K. Kikuchi, M. Yaegashi, Y. Tateyama, A. Yamada, *J. Am. Chem. Soc.* **2014**, *136*, 5039–5046.
- [62] D. G. Kwabi, T. P. Batcho, C. V. Amanchukwu, N. Ortiz-Vitoriano, P. Hammond, C. V. Thompson, Y. Shao-Horn, *J. Phys. Chem. Lett.* **2014**, *5*, 2850–2856.
- [63] S. Xu, R. Xu, T. Yu, K. Chen, C. Sun, G. Hu, S. Bai, H.-M. Cheng, Z. Sun, F. Li, *Energy Environ. Sci.* **2022**, *15*, 3379–3387.
- [64] X. Tang, S. Lv, K. Jiang, G. Zhou, X. Liu, *J. Power Sources* **2022**, *542*, 231792.
- [65] K.-H. Chen, K. N. Wood, E. Kazyak, W. S. LePage, A. L. Davis, A. J. Sanchez, N. P. Dasgupta, *J. Mater. Chem. A* **2017**, *5*, 11671–11681.

---

Manuscript received: October 15, 2024  
Revised manuscript received: November 15, 2024  
Accepted manuscript online: November 19, 2024  
Version of record online: November 28, 2024

---